Flexible, Graphene-Coated Biocomposite for Highly Sensitive, Real-Time Molecular Detection

*Lili Wang, Joshua A. Jackman, Wei Beng Ng, and Nam-Joon Cho**

Wearable biosensors hold significant potential for healthcare and environmental applications, and the development of flexible and biocompatible sensing platforms for high accuracy detection of physiological biomarkers remains an elusive goal. Herein, an ultrasensitive, flexible sensor is described that is based on a 3D hierarchical biocomposite comprised of hollow, natural pollen microcapsules that are coated with a conductive graphene layer. Modular assembly of the graphene-coated microcapsules onto an ultrathin polyethylene terephthalate layer enables a highly flexible sensor configuration with tunable selectivity afforded by subsequent covalent immobilization of antibodies against target antigens. In a proof-of-concept example, the biosensor demonstrates ultrahigh sensitivity detection of prostate specific antigen (PSA) down to 1.7×10^{-15} M with real-time feedback and superior performance over conventional 2D graphene-coated sensors. Importantly, the device performance is consistently high across various bending conditions. Taken together, the results demonstrated in this work highlight the merits of employing lightweight biocomposites as modular building blocks for the design of flexible biosensors with highly responsive and sensitive molecular detection capabilities.

1. Introduction

Biosensors enable the conversion of biological functions (e.g., protein–protein molecular interactions) into functional readouts (e.g., change in electrical, optical, or mechanical properties) that facilitate a wide range of practical applications from healthcare diagnosis to environmental monitoring.[1] In conventional formats, nanomaterial-based biosensors with design features on the same length scale as the target biological molecules have been developed on rigid substrates, with the most common example being silicon nanowires on silica.[2] While such approaches enable ultrasensitive, multiplexed real-time detection, fundamental design strategies based on rigid substrates are incompatible with growing trends toward flexible biosensors that can be interfaced with complex biological interfaces (e.g., skin, teeth).[3] Hence, there is significant potential for exploring the design of nanomaterial-based biosensors with flexible configurations for the development of wearable point-of-care devices.

One of the most promising design options involves combining 3D topographical structures with surface functionalization strategies in order to increase the available surface area for analyte binding and thereby facilitate high sensitivity measurements while also enabling high selectivity for the target molecule.[4] In this regard, natural materials that exhibit lightweight and durable characteristics are highly desirable as template structures, and pollen microcapsules are a particularly ideal candidate due to their highly monodisperse character, facile functionalization through various surface chemistries, and wide abundance.[5] Indeed, we have recently explored the feasibility of graphene-coated pollen microcapsules as high-performance actuating elements within ultrahigh sensitivity biosensor configurations on a rigid substrate.[6] Extending such capabilities to flexible substrates would represent a key step toward validating this sensing approach for highly selective and robust molecular detection in demanding applications.[3a,7] In particular, flexible biosensors are growing in demand because they offer improved connectivity between living biological systems and sensor devices.[8] For example, wearable graphene biosensors have proven capable of extremely sensitive chemical sensing on biological surfaces (e.g., tooth surface).[3a,9] At the same time, the incorporation of natural design materials as components in flexible biosensors remains a largely unmet goal, with great potential for achieving high biocompatibility and biodegradability for in vivo applications.

Toward this goal, the objective of the present study is to develop a flexible biosensor based on modular assemblies of natural pollen microcapsules that are functionalized with reduced

Dr. L. L. Wang, Dr. J. A. Jackman, W. B. Ng, Prof. N.-J. Cho
School of Materials Science and Engineering
Nanyang Technological University
50 Nanyang Avenue, Singapore 639798
E-mail: njcho@ntu.edu.sg
Dr. L. L. Wang, Dr. J. A. Jackman, W. B. Ng, Prof. N.-J. Cho
Centre for Biomimetic Sensor Science
Nanyang Technological University
50 Nanyang Drive, Singapore 637553
Prof. N.-J. Cho
School of Chemical and Biomedical Engineering
Nanyang Technological University
62 Nanyang Drive, Singapore 637459
Dr. L. L. Wang
State Key Laboratory on Integrated Optoelectronics
College of Electronic Science and Engineering
Jilin University
Changchun 130012, P.R. China

DOI: 10.1002/adfm.201603550

graphene oxide (rGO) coatings, thereby enabling selective and real-time detection of protein biomarkers at extremely low analyte concentrations. By utilizing rGO-coated sunflower pollen (SFP) particles that are functionalized with antibodies as modular building blocks, a hierarchical 3D assembly of rGO@SFP microcapsules is established on a flexible substrate for molecular detection applications, with proof-of-concept demonstration to measure the solution concentration of prostate specific antigen (PSA), which is a biomarker that can be used to diagnose prostate cancer among males.[10] Importantly, the rGO@SFP-based biosensor not only demonstrated the lowest PSA limit of detection (1.7×10^{-15} M) reported to date but also maintained similar levels of sensing performance across various bending conditions.

2. Results and Discussion

2.1. Design of Flexible rGO@SFP-Based Biosensor

The fundamental operation and key functionalities of the rGO@SFP-based biosensor design are schematically illustrated in **Figure 1**. The sensing element is based on a field-effect-transistor (FET) measurement configuration whereby target analyte binding induces a charge-transfer, which causes a change in the electrical conductivity of the rGO@SFP sensing layer (Figure 1a). The relative current change is expected to be proportional to the analyte concentration and can therefore be used to estimate the level of cancer marker in solution. Toward this design goal, a pair of Au (100 nm in thickness)/Pt (10 nm in thickness) source and drain electrodes are first deposited on a flexible ultrathin polyethylene terephthalate (PET) substrate using an electron beam evaporator with a predetermined shadow metal mask (Step I in Figure S1, Supporting Information). Next, electroactive rGO@SFP microcapsules are deposited on the flexible substrate via spin-coating (Step II in Figure S1, Supporting Information). The 3D topographical structure of the hybrid rGO@SFPs sensing elements facilities a large surface area to bind the target analyte.[11] Highly selective detection is enabled by functionalizing the rGO surface with immobilized monoclonal antibodies that recognize the target analyte, in this case PSA, which is a widely studied prototype biomarker and provides a molecular signature for diagnosis of prostate cancer (Step III in Figure S1, Supporting Information).[12] Figure 1b presents the covalent functionalization scheme to attach anti-PSA antibodies onto the surface of rGO@SFP microcapsules. First, carboxylic acid functional groups on the rGO surface are activated[13] by using 1-ethyl-3-(3-dimethylaminopropyl) carbodiimide hydrochloride (EDC) and *N*-hydroxysulfosuccinimide (Sulfo-NHS) as coupling agents.[14] Next, the anti-PSA antibodies are incubated with the activated surface and a substitution reaction takes place whereby the amine functional groups of the protein form an amide bond with the rGO surface, thus facilitating covalent protein attachment.[15] Hence, the covalently attached antibody constitutes the sensor recognition element for PSA molecular detection.

2.2. Characterization of rGO@SFP Sensing Materials

As illustrated in **Figure 2**, SFPs with an urchin-like hierarchical structure were extracted from *Helianthus annuus* spores

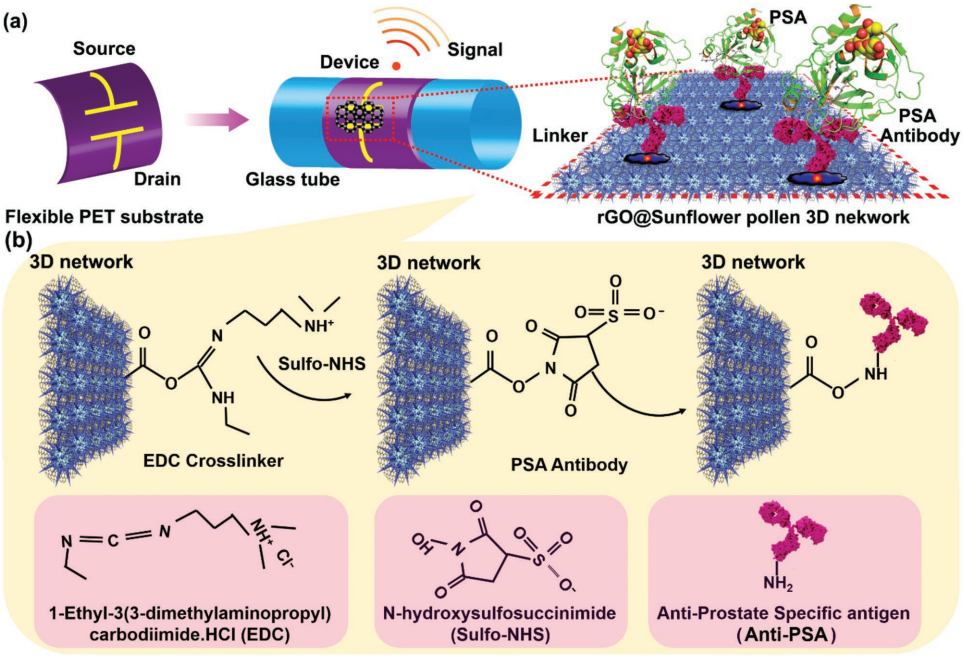

Figure 1. Design scheme of a flexible biosensor with graphene-functionalized pollen microcapsules as the sensing element for molecular detection. a) Schematic illustration of the flexible biosensor fabrication procedure. Ultrathin PET substrates were patterned with Au/Pt electrodes by evaporation. Next, rGO@SFP sensing films were deposited over a flexible PET substrate via a spin-coating procedure. The individual microcapsules are functionalized with anti-PSA antibodies which recognize the target analyte. b) Conjugation scheme for attachment of anti-PSA antibody to the rGO@SFP microcapsules through EDC/NHS chemistry.

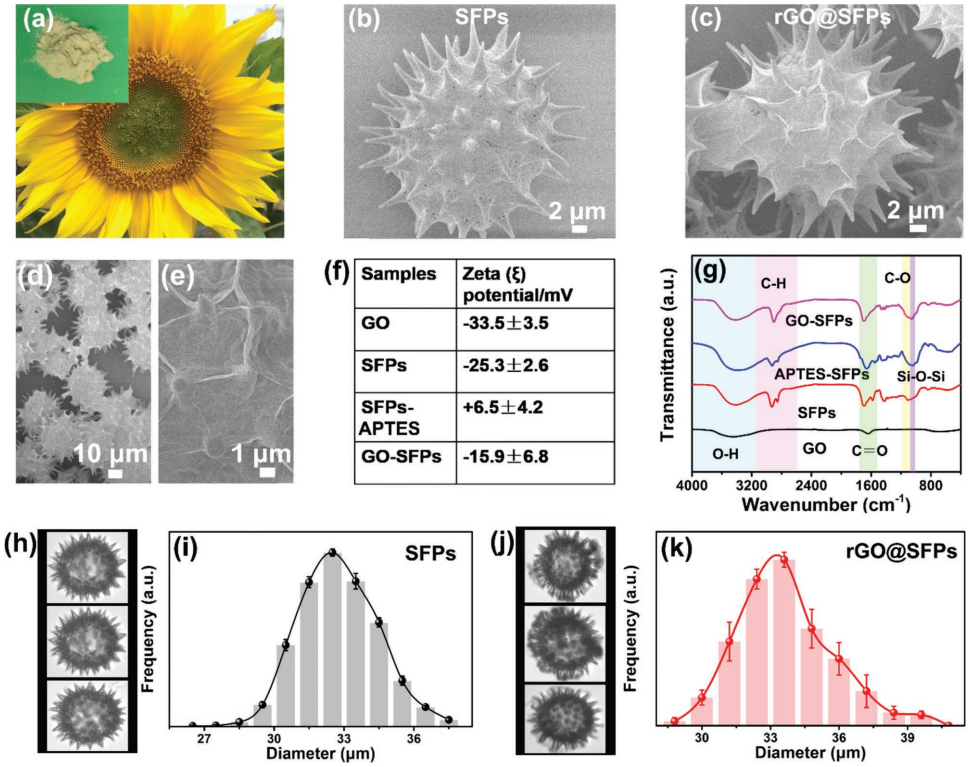

Figure 2. Structural characterization of rGO@SFP microcapsules. a) Optical images of SFP extraction (inset) from *Helianthus annuus* plants. FESEM images of b) SFPs and c–e) rGO@SFP microcapsules. f) Zeta potential values and g) FTIR spectra during various stages of rGO@SFP capsule fabrication. h,i) DIPA optical images and corresponding size histogram for pristine SFPs. j,k) DIPA optical images and corresponding size histogram for rGO@SFPs. Error bars show the standard deviation for $n = 3$ measurements.

(Figure 2a,b; Figures S2 and S3 and Table S1, Supporting Information) and then functionalized with rGO sheets, yielding a 3D conductive network (Figure 2c; Figure S2, Supporting Information). rGO@SFPs were developed based on (3-aminopropyl) trimethoxysilane (APTES)-modified SFP capsules upon which graphene oxide (GO) sheets were attached via electrostatic attraction followed by a chemical reduction step with hydrazine. Field emission scanning electron microscope (FESEM) images of rGO@SFP samples show a well-defined, uniform assembly of rGO sheets with high surface coverage across the SFP surface (Figure 2c–e). The sheet attachment likely arises from strong electrostatic attraction between negatively charged GO sheets and positively charged APTES-functionalized SFPs, as confirmed by zeta (ζ) potential measurements and Fourier transform infrared (FTIR) spectroscopic experiments (Figure 2f,g).[16] Contact angle measurements confirmed the hydrophilic character of the APTES-functionalized SFPs (Figure S4, Supporting Information).

To further characterize the morphological properties of a large number (>1000) of individuals microcapsules, dynamic image particle analysis (DIPA) was also employed (Figure 2h–k). The SFP capsules exhibit a nearly spherical morphology, and hence their size can be approximated by calculating the equivalent spherical diameter. It is observed that the uncoated pollen capsules have an average diameter 32.5 ± 4.2 μm, whereas the rGO@SFPs have an average diameter of 33.6 ± 5.1 μm. This difference is attributed to the rGO coating on the SFP surface. The DIPA images further confirm the presence of the rGO coating based on the increased optical contrast of the coated SFPs versus the pristine SFPs (cf. Figures 2h and 2j). Another interesting feature of the coated SFPs is that they retain a hollow structure (Figure S5, Supporting Information).[4] The chemical properties of the rGO sheets on the rGO@SFP capsules were confirmed by Raman spectra measurements, and the brownish transparent solution turned black (Figure S6, Supporting Information). The intensity ratio of the D and G peaks (I_D/I_G) increased after rGO synthesis, verifying that the GO was successfully reduced to rGO.[17]

2.3. Establishment of the rGO@SFP Flexible Biosensor

Optical images of individual electrodes before and after deposition of rGO@SFP microcapsules onto the PET substrate by spin-coating are shown in **Figure 3**a,b. The device consists of gold source and drain electrodes that are connected to form a channel with around 100 μm width (Figure 3a and Figure S7, Supporting Information). The deposited rGO@SFPs are interconnected and form a 3D conductive network (Figure 3b). An optical image of the device chip configured in a microfluidic poly(dimethylsiloxane) (PDMS) flow cell is shown in Figure 3c. This flow cell is mounted directly on top of the rGO@SFP-coated sensing layer. The sensing measurements were conducted in flow-through mode (Figure 3d). As presented in

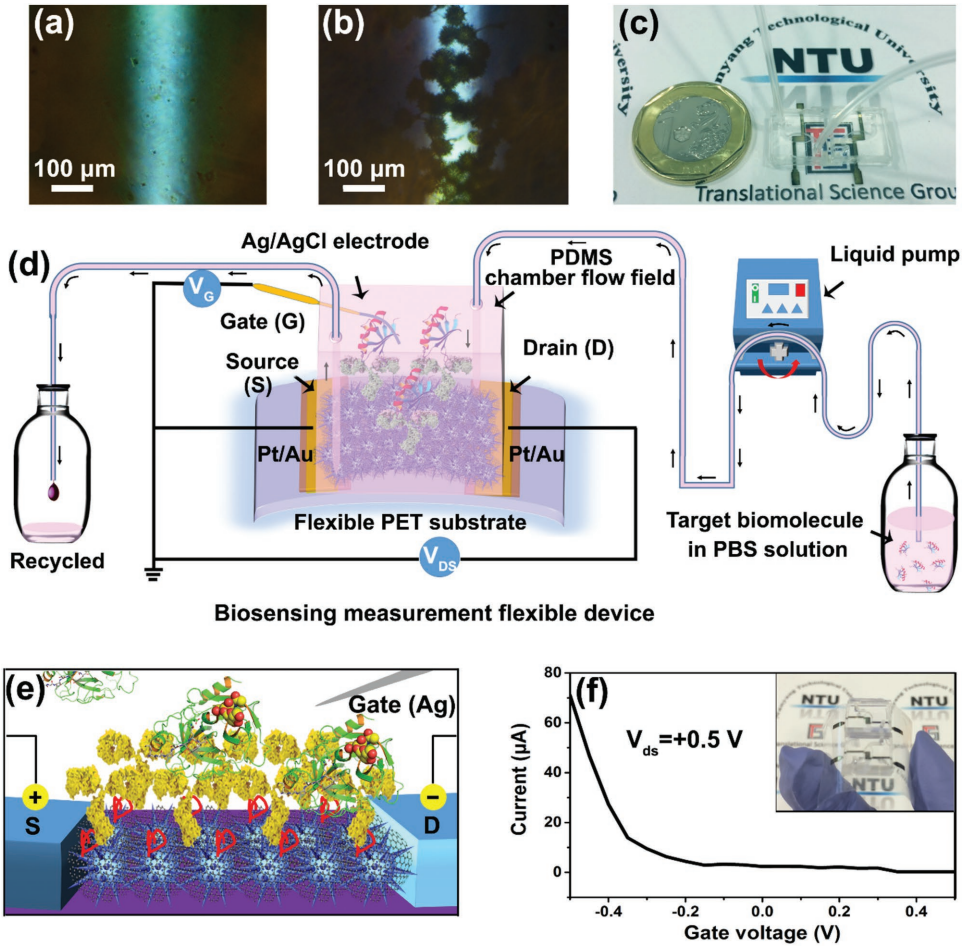

Figure 3. Characterization of rGO@SFP biosensor. a,b) Optical microscope images of the electric channel before and after deposition of rGO@SFP sensing film. c) Photograph and d) schematic diagram of the biosensor configuration with microfluidic flow cell. e) Schematic diagram of the biosensor upon target PSA binding. f) Gating effect of the rGO@SFP-based biosensor with V_{ds} = +0.5 V.

Figure 3e, the biosensor is able to detect the target PSA based on changes in the surface potential and corresponding effects on the electrical conductance signal. Figure 3f presents the relationship between the source-drain current and the gate potential of the rGO@SFP biosensor. The observed gating effect agreed well with the p-type behavior of rGO thin-film transistors, which exhibit a decrease in conductance when a positive gate potential is applied.[18]

2.4. Real-Time Detection of PSA Target

Electrochemical biosensing is a rapid and convenient platform to detect electrical signals from the direct conversion of molecular binding events.[19] In general, depending on the charge carriers in the semiconductor channel (electrons for an n-type channel and holes for a p-type channel), the direction of the conductance change is determined by the electrical charge properties of the target antigen, and the magnitude of the change in conductance is proportional to the antigen–antibody interaction.[19b] In this work, the surface-deposited rGO@SFP capsule network exhibits p-type behavior. PSA is negatively charged in phosphate-buffered saline (PBS, pH 7.4) due to an isoelectric point of ≈6.8,[20] and will therefore induce negative potential gating effects.[21] As a result, PSA binding is expected to increase the hole density in the rGO@SFP layer, and ultimately lead to an increase in electrical current (**Figure 4**a).[19b,20b,22] Owing to this expected result, we monitored the change in current signal as the sensing basis for PSA detection.[19a]

We next compared the conductance signals generated by nonspecific (no immobilized antibody) and specific (immobilized antibody) PSA binding to the sensor surface. Figure 4b,c shows the kinetic measurement data for target PSA binding in 10×10^{-3} M PBS (pH 7.4). Significantly, 250×10^{-15} M PSA binding to the antibody-coated sensor surface yielded a ≈50% increase in current signal while binding to the noncoated sensor surface resulted in a negligible response. Moreover, the antibody-coated sensor surface had much lower current noise, resulting in a more stable sensing signal and thereby enabling high sensitivity. The response time presented in Figure 4 (defined as the time point to reach 90% current change in the presence of target protein) shows that the biosensing scheme detected 1×10^{-12} M target PSA within 4 s, which is a 3–4 order

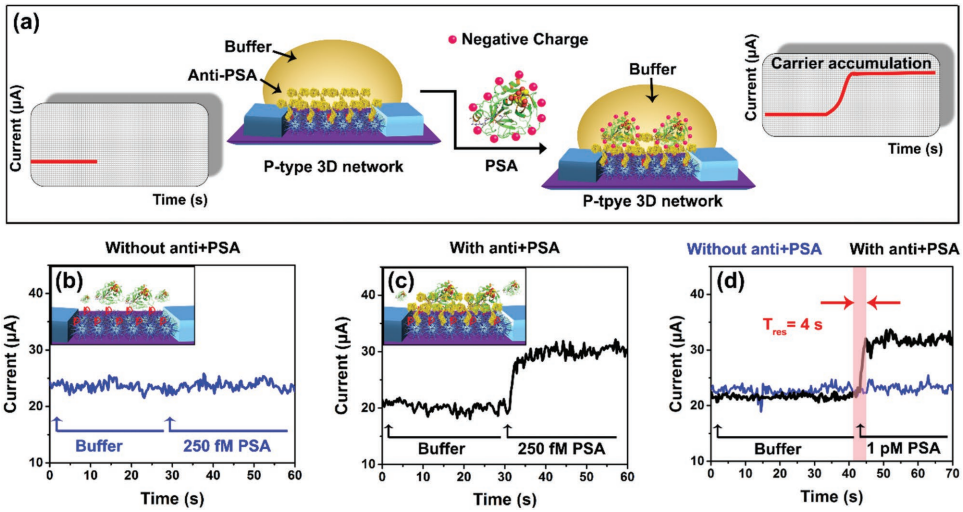

Figure 4. Sensor detection of PSA analyte. a) Schematic illustration of current change mechanism for detecting target PSA molecules attached to the sensor surface. b,c) Kinetic monitoring of PSA binding to rGO@SFP-based biosensor without and with immobilized anti-PSA antibodies. d) Response time of rGO@SFP-based biosensor detection against 1×10^{-12} M target PSA.

improvement over an antibody-coated platform consisting of 2D rGO sheets on a PET substrate (Figure S8, Supporting Information).

Figure 5a presents real-time sensitivity curves (percentage relative change in current, defined as $\Delta I/I_0$, where ΔI represents the change of the current in the measurement response, and I_0 represents the initial current signal) of the rGO@SFP-based biosensor in the presence of increasing PSA solution concentrations from 1.7×10^{-15} M to 1×10^{-9} M. Higher steady-state current responses were obtained and the sensitivity increased with increasing target PSA concentration. Figure 5b depicts the measurement sensitivity as a function of the target PSA concentration. The curve shows nonlinear behavior with respect to the concentration of target PSA, suggesting strong binding between immobilized antibodies and attached PSA biomolecules.[23] The lowest detectable PSA concentration level was 1.7×10^{-15} M, with an increase in relative current change (about 3.2%) that exceeds the clinical detection limit (0.1 ng mL^{-1}, or ≈30.3×10^{-12} M) for PSA.[24] As presented in **Table 1**,[21,22,25] this result demonstrates the lowest reported limit of detection (LOD, 1.7×10^{-15} M) for PSA in saline conditions as well as a rapid response time (4 s), thereby highlighting the merits of the biocomposite sensor design.

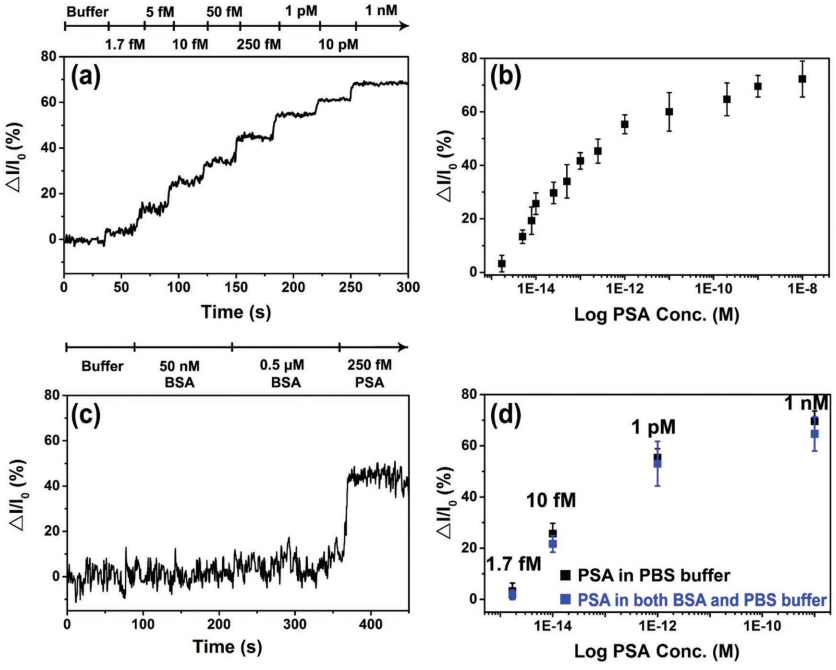

Figure 5. Measurement of electrical current response for the rGO-SFP-based biosensor for PSA detection. a) Real-time monitoring of relative conductance change (%) generated by introducing PSA at concentrations ranging from 1.7×10^{-15} M to 1×10^{-9} M. b) Dose-dependent responses to target PSA. Error bar shows the standard deviation for $n = 3$ measurements. c) Selective response of biosensor upon introduction of 50×10^{-9} M BSA, 0.5×10^{-6} M BSA, and 250×10^{-15} M PSA. d) Selective responses against target PSA in PBS (black square) and PBS + 0.5×10^{-6} M BSA (blue square). Error bar shows the standard deviation for $n = 3$ measurements.

In order to assess detection selectivity, competitive binding studies were conducted with target PSA and bovine serum albumin (BSA) (Figure 5c). No current change was detected in 50×10^{-9} M BSA despite a much higher protein concentration. Even at a high BSA concentration (0.5×10^{-6} M), the device still showed no significant measurement response. In marked contrast, a sizeable and rapid change in current was recorded upon introduction of a mixture of 250×10^{-15} M PSA and 0.5×10^{-6} M BSA, indicating high selectivity of the biosensor. Even in the presence of a very high BSA concentration (0.5×10^{-6} M), the LOD of target PSA remained 1.7×10^{-15} M and the relative

Table 1. Comparison of PSA biosensor performance.

Sample	Analyte	LOD	Solution	Detection time [s]	Reference
This work	PSA	1.7×10^{-15} M	PBS, pH 7.4	4	–
Si nanowire	PSA	2.3×10^{-15} M	PBS, pH 7.4	500	[22]
Si nanowire	PSA	150×10^{-15} M	PBS, pH 7.4	1000	[25a]
Si nanowire	PSA	30.3×10^{-12} M	PBS, pH 7.6	400	[25b]
Pt nanoparticles	PSA	30.3×10^{-12} M	PBS, pH 7.4	20	[25c]
In_2O_3 nanowires	PSA	1.5×10^{-9} M	PBS, pH 7.6	500	[21]

current change was 2.9% (Figure 5d), indicating excellent sensitivity and selectivity of the rGO@SFP-based biosensor with a flexible substrate configuration.

2.5. Mechanical Properties of the rGO@SFP-Based Flexible Biosensor

In addition to high sensitivity and selectivity of the device, excellent mechanical properties are another key prerequisite for a flexible and wearable sensor.[26] The mechanical flexibility of the rGO@SFP-based biosensor was evaluated as a function of bending angle at various contortions (Figure S9, Supporting Information). Importantly, the electrical and morphological properties of rGO@SFPs did not exhibit significant changes at different bending angles from 0° to 50°. These results support that the rGO@SFP microcapsules coated on the flexible PET substrate have high mechanical stability taking advantage of the rGO material with excellent flexibility and SFP capsules with natural elasticity.[7,27] **Figure 6**a presents the measurement performance of the rGO@SFP-based biosensor in flat and bent (≈30°) states in response to 10×10^{-15} M PSA addition, and similar sensing performance is observed in both cases with highly reproducible responses. Indeed, across a range of tested PSA concentrations, the percentage of relative change in the current signal for the device in the flat state was 15.1%, 25.7%, and 47.1% for 5×10^{-15}, 10×10^{-15}, and 250×10^{-15} M PSA concentrations, respectively (Figure 6b, black line). In the bent state, the percentage relative of change in the current signal was 14.9%, 23.8%, and 44.2%, respectively, for the same tested PSA concentration, indicating similar device performance to the flat state (Figure 6b, red line). Figure 6c shows the relative change in the current signal as a function of target PSA concentration under different bending conditions. The results indicate that the relative change in current signal is similar across the different bent states. Moreover, the sensitivity of the rGO@SFP-based flexible biosensor increases nonlinearly with increasing target PSA concentration, which further indicates strong specific recognition between target PSA and anti-PSA. Finally, we measured the response selectivity of the device in the bent state for the PSA target versus incubation in PBS alone and exposure to an appreciably higher concentration of BSA (Figure 6d). As expected, the anti-PSA antibodies had much lower responses in the presence of BSA proteins or PBS solution alone. Hence, the rGO@SFP biosensor platform maintains high detection sensitivity and selectivity even in the bent state and is therefore a promising biocomposite to explore for wearable sensor applications.

3. Conclusion

In summary, we have developed a high-sensitivity flexible sensor composed of a 3D hierarchical biocomposite with a modular assembly design. The electroactive pollen capsule building blocks are deposited on a flexible PET substrate and demonstrate excellent sensing performance for PSA detection, with a 3–4 order of magnitude increase in measurement sensitivity versus conventional sensing strategies on 2D rGO films. Importantly, there was a 1.7×10^{-15} M limit of detection and fast response time of 4 s for PSA identification, with comparable sensing performance in the flat and bent states. Looking forward, our findings highlight the potential of employing natural biocomposites as a new design component for flexible and wearable sensors.

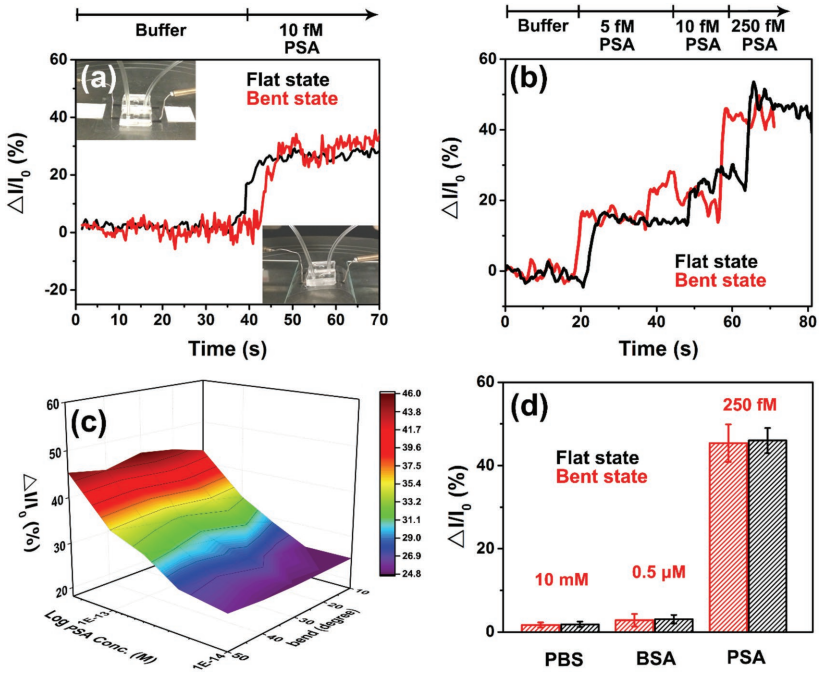

Figure 6. Demonstration of flexible biosensor performance for target PSA monitoring. a) Kinetic curves of the electrical current signal in response to 10×10^{-15} M PSA in the flat and bent states. Insets show optical images of the rGO@SFP-based flexible biosensor in the flat and bent states. b) Kinetic curves of the electrical current signal in response to different target PSA concentrations in the flat and bent states. c) Measurement response as a function of PSA concentration and the degree of substrate bending. d) Measurement responses in the flat and bent states in the presence of 10×10^{-3} M PBS, 50×10^{-9} M BSA, or 250×10^{-15} M PSA. Error bars show the standard deviation for $n = 3$ measurements.

4. Experimental Section

Materials: Potassium phosphate monobasic (KH_2PO_4), phosphoric acid (H_3PO_4), potassium chloride (KCl), hydrochloric acid (HCl), acetone (C_3H_6O), sodium hydroxide (NaOH), sodium chloride (NaCl), potassium hydroxide solution (KOH), isopropanol (IPA), sodium phosphate dibasic (Na_2HPO_4), ethanol (C_2H_5OH), hydrazine (35 wt%), toluene (C_7H_8), and (3-aminopropyl)trimethoxysilane (APETS, 98%) were purchased from Alfa Aesar, respectively. PSA protein and anti-prostate specific antigen antibody (anti-PSA antibody) were purchased from Abcam plc (UK). Perylene-3,4,9,10-tetracarboxylic dianhydride (97%) and GO (>95%) were purchased from Sigma-Aldrich.

Extraction of Natural H. annuus Spores: The SFP grains were obtained by the extraction process, including acidolysis and a series of washing process followed by vacuum drying.[5b,28] The *H. annuus* SFP grains (70 g) were first dispersed in 500 mL, 85%, phosphoric acid (H_3PO_4, v/v,) and stirred mildly to form a homogeneous suspension. The *H. annuus* grains were refluxed with gentle stirring at 70 °C for 5 h and then collected by filtration and rinsing at a high temperature of about 40–50 °C with distilled water, acetone, 2 M hydrochloric acid, 2 M sodium hydroxide, distilled water, acetone, ethanol, and distilled water, respectively. The resulting SFPs were dried under vacuum at 60 °C for 12 h and stored in a dry cabinet at 25 °C until experiment.

Preparation of the rGO@SFP Biomaterials: 10 mg of the SFPs was dispersed in 10 mL of toluene solvent to produce a 1 mg mL^{-1} stock solution. SFP/toluene and APTES (98%) solutions were combined to make a 200:1 (v:v) mixture and the mixture was then stirred under a constant stream of nitrogen gas for 24 h in order to obtain the APTES-modified SFP sample. Next, the solution of APTES-modified SFPs was prepared at a concentration of 1 mg mL^{-1}. APTES-modified SFPs (10 mL) were incorporated into a 20 mL aqueous solution including 0.5 mL of a 0.04 mg mL^{-1} GO sheets suspension along with moderate magnetic stirring for 6 h. The reduction of GO was then performed by the addition of 0.7 mL hydrazine (35 wt%), which converted GO to rGO. Finally, the rGO@SFP microcapsules were obtained by centrifugation and washing with water at 8500 rpm for 10 min.

Fabrication of Flexible rGO@SFP-Based Biosensor: The fabrication process of the biosensor followed the general steps outlined in the methods by Lieber and co-workers.[2a] 90 nm-thick Au electrodes (10 nm Pt was predeposited as an adhesion layer) were deposited on the flexible polyethylene terephthalate (PET) substrate by evaporation with a customized mask. The channel region was defined with a width (W) of about 100 µm and a length (L) of about 200 µm. 2 mg mL^{-1} of rGO@SFPs in a 50/50 v/v% mixture of ethanol and water was spin-coated onto the surface of the PET substrate with Pt/Au electrodes by two-step spinning at 500 rpm for 20 s followed by 3000 rpm for 40 s. Then, a PDMS flow cell with microfluidic channel was mounted directly on the central rGO@SFP-based sensing layer region of the biosensor. A peristaltic pump (ISM 833C, ISMATEC) was used to input/output solution from different vials through PharMed BPT biocompatible tubing along the arrow direction (cf. Figure 3d).

Fabrication of Flexible rGO-Based Biosensor: The fabrication process of flexible rGO-based biosensor was similar to that of the flexible rGO@SFP-based biosensor. The only difference was that 1.2 mg mL^{-1} of rGO sheets in a 50/50 v/v% mixture of ethanol and water were spin-coated onto the surface of the PET substrate with Pt/Au electrodes by two-step spinning at 500 rpm for 20 s and then 3000 rpm for 40 s.

Fabrication of mAB (Anti-PSA Antibodies) by Surface Modification: The obtained rGO@SFP-based biosensor was cleaned by oxygen plasma treatment. After that, the device was immersed into a perylene-3,4,9,10-tetracarboxylic acid aqueous solution (hydrolysis product of perylene-3,4,9,10-tetracarboxylic dianhydride) for 30 min in order to endow more carboxyl groups (–COOH) on the rGO surface. The devices were thoroughly washed with water, methanol, and acetone after incubation in a water bath. The carboxylic acid groups were then activated and stabilized in a solution of EDC and NHS for 15 min at room temperature, followed by thorough rinsing with water. Finally, an antibody-PSA solution (100 µg mL^{-1}) in 10×10^{-3} M PBS (pH 7.4, including 0.2 g L^{-1} of potassium chloride (KCl), 8 g L^{-1} of sodium chloride (NaCl), 0.24 g L^{-1} of potassium phosphate monobasic (KH_2PO_4), 4×10^{-3} M $NaCNBH_4$ solution, and 1.44 g L^{-1} of sodium phosphate dibasic (Na_2HPO_4)) was transferred onto the device in order to enable antibody immobilization on the sensor surface, followed by washing the surface with a gentle flow of 10×10^{-3} M PBS solution.

Characterization: FESEM 6340F (JEOL, Japan) was employed in order to measure the surface structure and morphology of all samples. The Raman spectra of the GO and rGO samples were acquired using a confocal Raman microscope (WITec, Ulm, Germany) with a 488 nm laser excitation, a spatial resolution of 1 µm, and an accumulation time of 3 s at each spot. The micromeritic properties (three independent measurements) of SFP and rGO@SFP samples were calculated by DIPA. The surface charge properties and FTIR spectrophotometer spectra of GO, SFPs, APTES-modified SFPs, and GO@SFP samples were evaluated by zeta (ζ) potential measurements (ZetaPals Analyzer, Brookhaven Instruments, Holtsville, NY; monochromatic laser: 658 nm) and a Thermo Nicolet Nexus 870 spectrometer operated in transmission mode with a deuterated triglycine sulfate KBr detector, respectively. Optical images of the electric channel of the flexible biosensor were obtained by using an optical microscope (Nikon Eclipse TS 100, Japan). Electrical measurements and properties of the fabricated rGO@SFP-based biosensors were performed by a Keithley 4200-SCS semiconductor characterization system with a probe station at room temperature. An Ag/AgCl wire was placed in contact with the liquid solution as a gate electrode. For contact angle measurements, a thin layer of SFPs was spread out on self-adhesive carbon tape on a glass slide. A 2 µL bead of water was slowly lowered onto the SEC-coated surface. The contact angle was measured using the Attension Theta Optical Tensiometer (Biolin Scientific Holding AB, Sweden) with OneAttension 1.0 software. Measurements were taken at the following settings: 0.7× magnification and 10 s at 12 FPS.

Supporting Information

Supporting Information is available from the Wiley Online Library or from the author.

Acknowledgements

This work was supported by the National Research Foundation (NRF-CRP10-2012-07) to N.-J.C. L.W. is grateful for financial support from the Natural Science Foundation Committee (NSFC, Grant No. 51502110) and the Postdoctoral Science Foundation of China (No. 2015M571361). The authors acknowledge Mr. Michael Potroz and Ms. Ee-Lin Tan for providing materials and valuable scientific discussion.

Received: July 14, 2016
Revised: September 15, 2016
Published online: November 15, 2016

[1] a) L. Wu, X. G. Qu, *Chem. Soc. Rev.* **2015**, *44*, 2963; b) N. Gao, W. Zhou, X. C. Jiang, G. S. Hong, T. M. Fu, C. M. Lieber, *Nano Lett.* **2015**, *15*, 2143.

[2] a) F. Patolsky, G. F. Zheng, C. M. Lieber, *Nat. Protoc.* **2006**, *1*, 1711; b) Y. Cui, Q. Q. Wei, H. K. Park, C. M. Lieber, *Science* **2001**, *293*, 1289.

[3] a) M. S. Mannoor, H. Tao, J. D. Clayton, A. Sengupta, D. L. Kaplan, R. R. Naik, N. Verma, F. G. Omenetto, M. C. McAlpine, *Nat. Commun.* **2012**, *3*, 8; b) Z. Lou, S. Chen, L. L. Wang, K. Jiang, G. Z. Shen, *Nano Energy* **2016**, *23*, 7; c) W. Gao, S. Emaminejad, H. Y. Y. Nyein, S. Challa, K. V. Chen, A. Peck, H. M. Fahad, H. Ota,

H. Shiraki, D. Kiriya, D. H. Lien, G. A. Brooks, R. W. Davis, A. Javey, *Nature* **2016**, *529*, 509.
[4] C. Huang, G. Yang, Q. Ha, J. X. Meng, S. T. Wang, *Adv. Mater.* **2015**, *27*, 310.
[5] a) R. C. Mundargi, M. G. Potroz, S. Park, H. Shirahama, J. H. Lee, J. Seo, N. J. Cho, *Small* **2016**, *12*, 1167; b) J. Seo, L. Wang, W. Ng, N.-J. Cho, *ChemNanoMat* **2016**, *2*, 414; c) S. C. Han, J. W. Lee, K. Kang, *Adv. Mater.* **2015**, *27*, 5506.
[6] L. Wang, W. Ng, J. A. Jackman, N.-J. Cho, *Adv. Funct. Mater.* **2016**, *26*, 2097.
[7] H. Lee, T. K. Choi, Y. B. Lee, H. R. Cho, R. Ghaffari, L. Wang, H. J. Choi, T. D. Chung, N. Lu, T. Hyeon, S. H. Choi, D.-H. Kim, *Nat. Nano* **2016**, *11*, 566.
[8] C. Z. Liao, C. H. Mak, M. Zhang, H. L. W. Chan, F. Yan, *Adv. Mater.* **2015**, *27*, 676.
[9] Y. S. Rim, S. H. Bae, H. J. Chen, J. L. Yang, J. Kim, A. M. Andrews, P. S. Weiss, Y. Yang, H. R. Tseng, *ACS Nano* **2015**, *9*, 12174.
[10] a) X. Li, Y.-P. Zhang, H.-S. Kim, K.-H. Bae, K. M. Stantz, S.-J. Lee, C. Jung, J. A. Jiménez, T. A. Gardner, M.-H. Jeng, *Cancer Res.* **2005**, *65*, 1941; b) S. A. Hammond, R. Lutterbuese, S. Roff, P. Lutterbuese, B. Schlereth, E. Bruckheimer, M. S. Kinch, S. Coats, P. A. Baeuerle, P. Kufer, *Cancer Res.* **2007**, *67*, 3927.
[11] P. T. Yin, S. Shah, M. Chhowalla, K.-B. Lee, *Chem. Rev.* **2015**, *115*, 2483.
[12] a) S. Loeb, W. J. Catalona, *Cancer Lett.* **2007**, *249*, 30; b) J. P. Kim, B. Y. Lee, J. Lee, S. Hong, S. J. Sim, *Biosens. Bioelectron.* **2009**, *24*, 3372.
[13] a) X. Wang, S. M. Tabakman, H. Dai, *J. Am. Chem. Soc.* **2008**, *130*, 8152; b) A. Ghosh, K. V. Rao, S. J. George, C. Rao, *Chem. Eur. J.* **2010**, *16*, 2700.
[14] A. M. Münzer, Z. P. Michael, A. Star, *ACS Nano* **2013**, *7*, 7448.
[15] M. B. Lerner, J. D'Souza, T. Pazina, J. Dailey, B. R. Goldsmith, M. K. Robinson, A. C. Johnson, *ACS Nano* **2012**, *6*, 5143.
[16] I. H. Gubbuk, M. Ozmen, E. Maltas, *Int. J. Biol. Macromol.* **2012**, *50*, 1346.
[17] G. P. Kotchey, B. L. Allen, H. Vedala, N. Yanamala, A. A. Kapralov, Y. Y. Tyurina, J. Klein-Seetharaman, V. E. Kagan, A. Star, *ACS Nano* **2011**, *5*, 2098.
[18] a) S. Myung, J. Park, H. Lee, K. S. Kim, S. Hong, *Adv. Mater.* **2010**, *22*, 2045; b) F. Chen, Q. Qing, J. Xia, J. Li, N. Tao, *J. Am. Chem. Soc.* **2009**, *131*, 9908.
[19] a) D. R. Thevenot, K. Toth, R. A. Durst, G. S. Wilson, *Biosens. Bioelectron.* **2001**, *16*, 121; b) K. I. Chen, B. R. Li, Y. T. Chen, *Nano Today* **2011**, *6*, 131.
[20] a) D. A. Armbruster, *Clin. Chem.* **1993**, *39*, 181; b) X. P. Gao, G. Zheng, C. M. Lieber, *Nano Lett.* **2009**, *10*, 547; c) A. M. Ward, J. Catto, F. Hamdy, *Ann. Clin. Biochem.* **2001**, *38*, 633.
[21] G. F. Zheng, F. Patolsky, Y. Cui, W. U. Wang, C. M. Lieber, *Nat. Biotechnol.* **2005**, *23*, 1294.
[22] C. W. Park, C. G. Ahn, J. H. Yang, I. B. Baek, C. S. Ah, A. Kim, T. Y. Kim, G. Y. Sung, *Nanotechnology* **2009**, *20*, 6.
[23] S. Myung, P. T. Yin, C. Kim, J. Park, A. Solanki, P. I. Reyes, Y. Lu, K. S. Kim, K. B. Lee, *Adv. Mater.* **2012**, *24*, 6081.
[24] D. A. Giljohann, C. A. Mirkin, *Nature* **2009**, *462*, 461.
[25] a) G. F. Zheng, X. P. A. Gao, C. M. Lieber, *Nano Lett.* **2010**, *10*, 3179; b) E. Spain, S. Gilgunn, S. Sharma, K. Adamson, E. Carthy, R. O'Kennedy, R. J. Forster, *Biosens. Bioelectron.* **2016**, *77*, 759; c) C. Li, M. Curreli, H. Lin, B. Lei, F. N. Ishikawa, R. Datar, R. J. Cote, M. E. Thompson, C. W. Zhou, *J. Am. Chem. Soc.* **2005**, *127*, 12484.
[26] a) J. H. An, S. J. Park, O. S. Kwon, J. Bae, J. Jang, *ACS Nano* **2013**, *7*, 10563; b) W. Li, J. Wang, J. Ren, X. Qu, *Angew. Chem., Int. Ed.* **2013**, *52*, 6726; c) Z. Lou, G. Z. Shen, *Adv. Sci.* **2016**, *3*, 19.
[27] C. Lee, X. Wei, J. W. Kysar, J. Hone, *Science* **2008**, *321*, 385.
[28] R. C. Mundargi, M. G. Potroz, J. H. Park, J. Seo, J. H. Lee, N. J. Cho, *RSC Adv.* **2016**, *6*, 16533.